A Comparison of Front-End Amplifiers for Tetrapolar Bioimpedance Measurements

Panagiotis Kassanos, *Member, IEEE*, Florent Seichepine, and Guang-Zhong Yang, *Fellow, IEEE*

Abstract—Many commercial benchtop impedance analyzers are incapable of acquiring accurate tetrapolar measurements, when large electrode contact impedances are present, as in bioimpedance measurements using electrodes with micrometer-sized features. External front-end amplifiers can help overcome this issue and provide high common-mode rejection ratio (CMRR) and input impedance. Several discrete component-based topologies are proposed in the literature. In this article, these are compared with new alternatives with regard to their performance in measuring known loads in the presence of electrode contact impedance models, to emulate tetrapolar bioimpedance measurements. These models are derived from bipolar impedance measurements taken from the electrodes of a tetrapolar bioimpedance sensor. Comparison with other electrode models used in the literature established that this is a good and challenging model for bioimpedance front-end amplifier evaluation. Among the examined amplifiers, one of the best performances is achieved with one of the proposed topologies based on a custom front-end with no external resistors (AD8066/AD8130). Under the specific testing conditions, it achieved an uncalibrated worst-case absolute measurement deviation of 4.4% magnitude and 4° at 20 Hz, and 2.2% and 7° at 1 MHz accordingly with loads between 10 Ω and 10 kΩ. Finally, the practical use of the front-end with the impedance analyzer is demonstrated in the characterization of the bioimpedance sensor, in saline solutions of varying conductivities (2.5–20 mS/cm) to obtain its cell constant. This article serves as a guide for evaluating and choosing front-end amplifiers for tetrapolar bioimpedance measurements both with and without impedance analyzers for practical/clinical applications and material/sensor characterization.

Index Terms—Bioimpedance, front-end, impedance analyzer, instrumentation amplifier (IA), tetrapolar impedance measurement.

I. INTRODUCTION

TETRAPOLAR (four-point) impedance measurements are widely used in material and device characterization and sensor applications [1]–[7]. The latter typically involves bioimpedance measurements using tetrapolar electrode systems for the characterization of tissues (e.g., ischemia monitoring and cancer tissue identification) [1], [2]. An AC current is injected between a pair of electrodes, and the resulting voltage is measured by a second pair of electrodes [8]. The advantage of tetrapolar measurements is that since injecting and measuring leads are separated, the cable and, more importantly, the interfacial contact impedance between electrode and sample under test (SUT; e.g., tissue) are not included in the measurement. This is since there is no current flow through the voltage measurement leads. Interfacial impedance is dominant particularly at low frequencies and can be orders of magnitude larger than the actual SUT impedance, depending on the sample, frequency, and electrode system used. This becomes increasingly problematic as the size of electrodes shrinks down to microscales, since electrode impedance is inversely proportional to electrode area.

Impedance analyzers are often used for the characterization of samples and sensors [3], [9]–[11]. This generally serves as a means of establishing the expected impedance characteristics, necessary for the appropriate design of custom miniature portable electronics [1], [12]–[17]. Commercial benchtop analyzers are often based on the autobalancing pseudo-bridge and are designed to characterize two-terminal electronic components, such as resistors, inductors, and capacitors, which exhibit low contact impedances [18]. As discussed in [18] and [19], the operation of such instruments is based on the injection of a test signal with an output impedance of 50 Ω of a user-determined fixed frequency (f) or frequency range and fixed amplitude (V_{in}) to the SUT (Z_x) through the high current (H_{cur}) terminal, as in Fig. 1(a). This leads to the flow of a current (I_x) through the load and the establishment of a voltage (V_x) which is measured by the high potential (H_{pot}) terminal of the instrument. Most of this current flows through a current sense resistor (R_r) and to a voltage-controlled voltage source (VCVS) at the low current (L_{cur}) terminal. Some of the current (I_d) flows through a zero detector (ZD) at the low potential (L_{pot}) terminal, the output of which controls the VCVS, as shown in Fig. 1(a). This forces the current through L_{pot} and the potential of the terminal to go to 0 and all the current to flow through L_{cur}. In the characterization of two-terminal devices and in the absence of contact impedances, the instrument will be in a bipolar arrangement and L_{pot} and L_{cur} will be at the same potential. Knowledge of the potential across the current sense resistor and measurement of the potential at H_{pot} terminal allow the measurement of Z_x.

Interfacing the instrument with the SUT is achieved with test leads and fixtures, which introduce parasitics. Any consequent
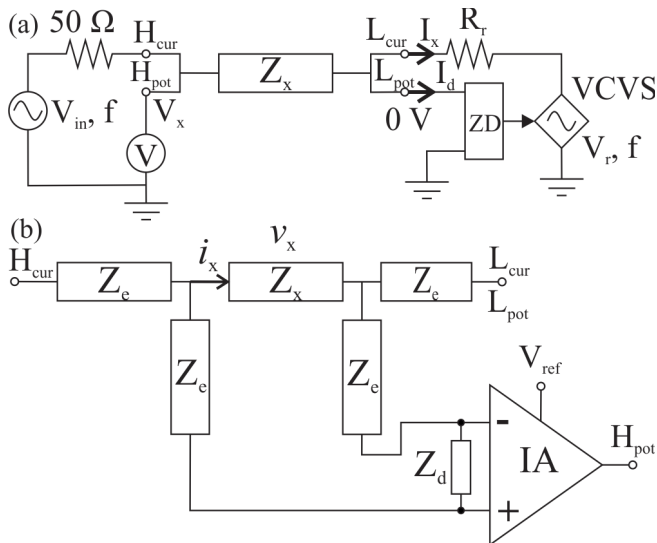
Fig. 1. (a) Autobalancing pseudo-bridge topology used in commercial benchtop impedance analyzers, in typical measurements, where contact impedance between the four leads (L_{pot}, L_{cur}, H_{pot}, and H_{cur}) and the device under test (Z_x) are negligible [18], [19]. (b) Use of a front-end amplifier for tetrapolar measurement with large contact impedances, as proposed in [23].

errors are calibrated by using open- and short-circuit reference measurements. The former measures the parallel stray admittance (Y_o), since $Z_s \ll 1/Y_o$ and the latter the series fixture residual impedance (Z_s). This, however, falls short when custom fixtures and external circuits (such as multiplexers and amplifiers) are used [18]–[20]. In such cases, an open/short/load compensation is applied, where a known calibration impedance is additionally used. The compensation procedure and equations are discussed in detail in [18]–[21].

In a tetrapolar arrangement, when measuring biomaterials, however, there will be large electrode contact impedances (Z_e) present at each terminal. This is shown in Fig. 1(b) by the addition of the four Z_e impedances at the terminals of Z_x, assuming for simplicity that all four are equal. If the H_{cur} and L_{cur} terminals are used to connect to the current injection electrodes and H_{pot} and L_{pot} are used to connect to the voltage measurement electrodes of a tetrapolar electrode system to measure the potential across Z_x, then L_{cur} and L_{pot} terminals will no longer be at the same potential due to the large Z_es. This leads to large measurement errors [4], [11], [18], [22]. In addition, the open/short/load compensation procedure typically performed applies only to bipolar measurements. An open/short/load compensation method suitable for tetrapolar measurements was presented in [18].

Guarding of the connecting cables is also important [10]. According to [19], an extended measurement range is achieved when the so-called four-terminal pair (4TP) configuration is implemented. In a 4TP configuration, the cable shields of the four terminals are shorted together at the vicinity of the measurement site. This reduces the mutual coupling between leads and the effect of stray capacitances between leads. The cable resistance combined with the contact impedance of the electrode with the SUT and the capacitance between cable core and shield form a low-pass filter, which attenuates and phase-shifts the potential at the H_{pot} terminal at high

frequencies. The low-pass filter formed at the L_{cur} terminals also leads to measurement errors [19]. It is thus important to keep cables as short as possible to minimize these.

To reduce the influence of electrode contact impedance, additional external front-end amplifiers are used to improve the input specifications of commercial instruments when used for bioimpedance applications [3]–[5], [9], [10], [18], [22], [23]. This involves the use of an instrumentation amplifier (IA), with high input impedance, to convert the differential voltage between the voltage measuring electrodes into a unipolar voltage that can be measured by the instrument. However, as highlighted in [24], the finite differential mode (DM) input impedance (Z_d) of the recording amplifier leads to nonlinear voltage loading effects and thus errors in the measurement of the voltage (v_x) across Z_x due to a current i_x [Fig. 1(b)]. Neglecting the common-mode (CM) input impedance and assuming for simplicity that the measuring electrode impedances are matched and equal to Z_e, according to [24], the recorded voltage is equal to

$$v_x = i_x Z_x \frac{Z_d}{Z_d + Z_x + 2Z_e}. \tag{1}$$

Z_x and Z_e can vary depending on the application, as a function of time and frequency. As discussed in [24] and [25], the limited input impedance degrades the overall CM rejection ratio (CMRR). Current sinking through the amplifier will lead to an unwanted voltage drop across Z_e. If Z_es are unequal, as is typically the case, this unwanted potential drop will be converted into a differential-mode signal from a CM one and thus into a CM error signal [26]. In contrast to electrophysiological signal recordings [27], in bioimpedance measurements, the main CM interference is at the measurement signal frequency, and it is produced by the current injected into the tissue [24], [28]. It cannot thus be removed by filtering or shielding [29]. The current injection electrode impedances, thus, introduce a large CM voltage [10]. A discussion on the CM voltage with regard to the current injection modality used can be found in [25], while CM errors are discussed in detail in [24], [25], and [29]. A high CMRR is essential to reject large CM signals and to tolerate degradation of the overall CMRR due to mismatched contact impedances [10], [24], [30].

The majority of the proposed front-ends are based on the design and setup recommended in [23], where the L_{pot} and L_{cur} terminals are shorted together. The IA drives the H_{pot} terminal and the H_{cur} and L_{cur} terminals drive the current injecting electrodes of the tetrapolar system, as shown in Fig. 1(b). Thus, H_{pot} continues to measure the potential across Z_x, since L_{cur} and L_{pot} are shorted and at virtual ground potential. The reference terminal of the IA is grounded.

In this article, various front-end amplifier topologies proposed in the literature are compared with a number of new alternative topologies with regard to their frequency response and characteristics (Section II). In Section III, a tetrapolar bioimpedance sensor, fabricated via a standard printed circuit board (PCB) manufacturing process, is characterized using saline solutions to obtain equivalent RC contact impedance models. Measurements of resistive loads in the presence of these models are used in Section IV to evaluate front-end performance in carrying out tetrapolar resistance measurements

<div style="text-align:center">

TABLE I
DIFFERENTIAL STAGE AND IA CHARACTERISTICS

</div>

Amplifier	BW (MHz)	DM Input Z	CM Input Z	dc CMRR (dB)	1 MHz CMRR (dB)	Input Current (μA)
INA111	2	1 TΩ 6 pF	1 TΩ 3 pF	90	16	2×10^{-6}
AD8421	10	30 GΩ 3 pF	30 GΩ 3 pF	100	44	1×10^{-4}
AD830	40	370 kΩ 2 pF	NA	100	74	5
AD8130	270	6 MΩ 3 pF	4 MΩ 4 pF	100	74	0.5
MAX435	275	800 kΩ	NA	90*	77*	1
AD8065	155	1 TΩ 4.5 pF	1 TΩ 2.1 pF	100*	68*	1×10^{-6}

Typical case data from the component data sheets.
AD8421 and INA111 data are for ±15 V power.
AD8065 data are for 5 V single supply.
CMRR data are from LTSpice simulations, except those marked with *.
AD8432 data are for the BR grade.

with a commercial impedance analyzer. In Section V, the sensor is characterized with tetrapolar measurements in saline solutions of varying conductivity with the selected front-end topology. The results are discussed in Section VI. Section VII provides the conclusion. The results of the study are useful for extending the capabilities of commercial impedance analyzers used for material and device characterization and also for the development of front-ends of custom impedimetric systems not relying on impedance analyzers [1], [14], [15].

II. FRONT-END AMPLIFIERS

Front-end amplifiers can generally take two forms. They can either be based on single-chip solutions, which have the advantage of a smaller footprint, or custom topologies using multiple chips. The differential mode (DM) and CM input impedances as well as the input bias current of single chip solutions and of the input buffer amplifiers of custom solutions are critical to ensure that there is minimal current flow to the amplifier inputs. As discussed in the introduction and in [10], [22], [24], [28], [29], and [31], a high CMRR is essential throughout the bandwidth (BW) of interest for differential amplifiers used for bioimpedance measurements. Since the amplifiers are set to a gain of 1 V/V and since the impedance analyzer used in this study measures from 20 Hz onward, amplifier offsets are not critical in this case. The amplifier BW is, however, critical and must be sufficiently high and flat within the frequency range of interest for bioimpedance measurements. This must also be such, so that that it does not introduce additional phase measurement errors. The characteristics of the commercial electrical components examined in this article are extracted from the manufacturer data sheets and LTSpice simulations and are summarized in Tables I and II. Additional information can be found in the respective component's data sheet.

A. Single Chip Solutions

In recent years, a wide range of monolithic three op-amp-based IAs have been made available in the market. Their advantage is that a single chip is needed, and a single external component is required to set the gain, while all other

<div style="text-align:center">

TABLE II
INPUT BUFFER AMPLIFIER CHARACTERISTICS

</div>

Amplifier	BW (MHz)	DM Input Z	CM Input Z	Input Bias Current (μA)
EL2244	120	150 kΩ//1 pF	15 MΩ	2.8
AD843	34	10 GΩ//6 pF	NA	50×10^{-6}
LT1498	10.5	5 pF	NA	250×10^{-3}
AD8066	155	1 TΩ//4.5 pF	1 TΩ//2.1 pF	1×10^{-6}
LMP7721	17	NA	NA	3×10^{-9}

Worst-case data from the component data sheets
EL2244 and AD843 data are for a ±15 V power supply
LT1498 and LMP7721 data are for a single 5 V supply

passive components are on-chip for accurate matching and hence high CMRR. Consequently, this leads to a more compact PCB design.

One such device (INA111 from Texas Instruments) was used in [22] with a Quadtech 1920 precision LCR meter (Table I). Another approach involves the use of AD8130 by Analog Devices, a differential difference amplifier (DDA) (Table I). The use of this component as a front-end for bioimpedance measurements with an Agilent 4294A impedance analyzer was demonstrated in [3]. DDAs have attracted interest in biomedical and sensor applications as IAs [27], [32]. A higher performance three op-amp-based single chip IA is AD8421 by Analog Devices (Table I). In this article, this IA is considered as an alternative for single chip solutions. It uses a precision current-feedback input stage followed by a difference stage. The former is implemented with superbeta bipolar transistors and bias current compensation that lead to the high input impedance and low input bias current reported in Table I.

B. Custom Topologies

Custom three op-amp IA topologies offer the freedom to build tailor-made IAs for specific applications. A unity gain is typically used for impedance analyzer front-ends, and the input stage of the three op-amp IAs can be configured as two unity gain buffers. Two such amplifiers are discussed in [10]. The first design was composed of two bipolar technology-based (EL2244 by Renesas) buffers (with a low input impedance) followed by an open-loop transconductance amplifier (MAX435 by Maxim Integrated). This topology will not be considered in this article as the components are dated and unavailable. The second design was composed of two FET input buffers (AD843, see Table II) and a DDA (AD830, see Table I), both by Analog Devices. A similar approach was more recently implemented in [4], where the rail-to-rail input and output bipolar LT1498 by Linear Technologies was used instead to implement the input buffers (Table II). This design is shown in Fig. 2(a). Another such solution using the rail-to-rail output AD8065 and AD8066 (Tables I and II) from Analog Devices was proposed in [9] and is shown in Fig. 2(b). This amplifier uses a laser-trimmed JFET stage and an auxiliary bipolar input stage allowing rail-to-rail-like input operation. It uses input buffers and a difference stage requiring highly matched resistors.

The second amplifier proposed in this article is based on the use of AD8066 for the implementation of the input buffers and the AD8130 DDA for the differential stage, as shown in Fig. 2(c). Alternatively, the AD8066 can be replaced with
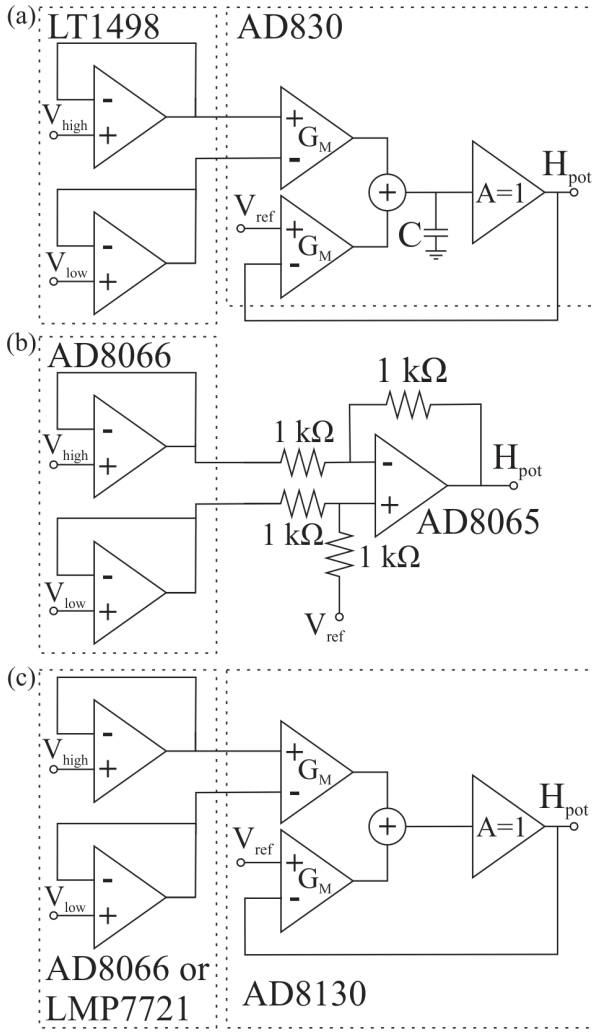
Fig. 2. (a) IA topology used in [4], based on the design proposed in [10]. (b) IA topology used in [9], similar to [23]. (c) New design using a DDA and high input impedance buffers (either AD8066 or LMP7721), similar to that of [10].

the LMP7721 by Texas Instruments (Table II), leading to the final topology that will be examined, as shown in Fig. 2(c).

C. Implementation

All amplifiers were incorporated into a single custom PCB, designed in Altium Designer (Altium Ltd., NSW, Chatswood, Australia) and manufactured by Eurocircuits (Mechelen, Belium). The PCB used 100-μm track widths and spacings, a symmetrical layout a compact design to minimize parasitics and approximately the same distances between input and output pins to PCB edge connectors to make them as similar as possible among all amplifiers. There are parasitic capacitances between amplifier inputs through the PCB FR4 substrate and between amplifier inputs and outputs to ground. Consequently, different topologies and components are characterized under the same conditions with regard to PCB parasitics. The impedance analyzer measures from 20 Hz onward and the amplifiers are set at unity gain. Consequently, large DC voltages due to electrode polarization that can saturate amplifiers with large gains are not an issue in this case. For the same reasons, amplifier offsets are also

not an issue. The option to use DC-blocking capacitors at the amplifier inputs and the necessary biasing resistors to ground forming high-pass filters, as well as DC-blocking capacitors at the amplifier outputs, were incorporated into the PCB design. Nevertheless, these were not used due to the aforementioned reasons. However, these should be taken into consideration, when using any of these amplifiers with full-custom instrumentation. For example, a T-network with 10-MΩ resistors following 1-μF capacitors was used in [33]. This provided a path for the input bias currents of the input buffers, as well as high differential and CM input impedances. No additional input or protection circuits or components were used, as in [3]–[5], [10], [12]–[15], [18], [22], and [23]. Operation beyond the absolute maximum ratings of the components is not expected, thus each component's protection circuitry was deemed to be sufficient for our application; neither are radio frequency interference issues relevant.

The front-end amplifier PCB was powered by the LM317 and LM337 voltage regulators using the decoupling capacitor values suggested in their data sheets, while the common ground was shorted with that of the wiring guards and the amplifier V_{ref} terminals. A supply of ± 5 V was used for all components apart from INA111 that was supplied with ± 6 V. The power supply terminals of each chip were decoupled with 100-nF ceramic multilayer capacitors, and additional decoupling was provided by 10-μF tantalum capacitors. A voltage of ± 9 V was supplied to the regulators via an Aim TTi EL302RT power supply. The various front-end amplifiers were characterized by applying a peak-to-peak sine wave signal of 500 mV at 43 frequencies between 20 Hz–10 MHz from an Aim-TTi TGA12104 signal generator to the noninverting input of the amplifier using a coaxial cable, while the inverting input was grounded. For the AD8421, INA111, and the amplifier of Fig. 2(a), a peak-to-peak 100-mV signal was used, from 3, 1.5, and 2.5 MHz onward, respectively, for each amplifier. Larger inputs beyond the respective frequencies for each amplifier led to output signal distortion, due to a low slew rate. The input and output signals were recorded with an Agilent InfiniiVision MSO-X 3054A 500 MHz, 4 GSa/s oscilloscope directly from the unloaded outputs of the amplifiers using the oscilloscope probes. The oscilloscope was set for high-resolution measurements and the measurements were averaged 8192 times. The gain and phase versus frequency characteristics of various amplifiers are compared in Fig. 3(a) and (b).

D. CMRR Simulations

The CMRR of the amplifiers was obtained and evaluated using LTSpice (Analog Devices, Norwood, MA, USA) and models provided by the component manufacturers. The results are shown in Fig. 3(c). For the AD8066/AD8065, a worst-case simulation was performed, as in [34], to evaluate the effect of the resistor tolerances (0.01%) to the CMRR. This provided the three different curves of Fig. 3(c). These were verified using LTSpice Monte Carlo simulations.

III. BIOIMPEDANCE SENSOR CHARACTERIZATION

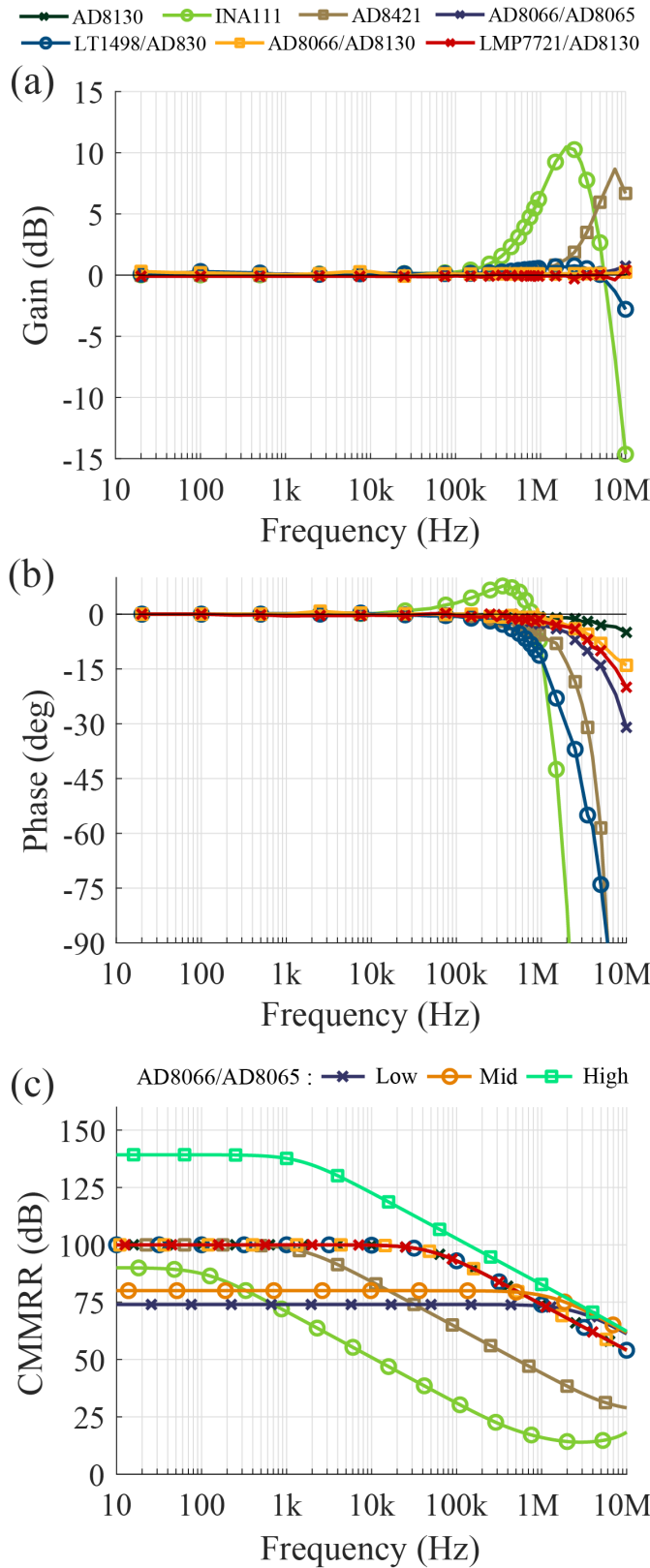In this work, the tetrapolar bioimpedance sensor design presented in [1] and incorporated in [35] was examined and
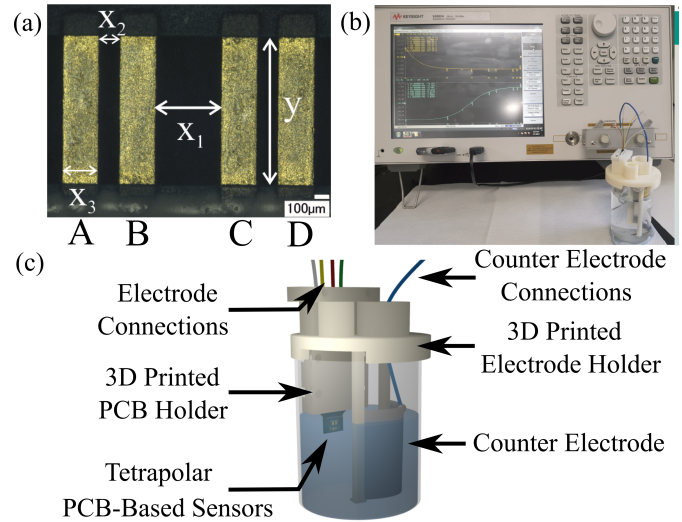
Fig. 4. (a) Tetrapolar bioimpedance electrode array used in this study. (b) Experimental set-up, showing the E4990A impedance analyzer, the 16047E fixture, and the 3-D-printed electrode support. (c) Schematic illustration of the custom 3-D-printed electrode support. The tetrapolar PCB-based impedance sensor is kept in place by a bespoke holder and the counter-electrode faces the PCB.

(as defined in [36]) within a specific tissue volume of interest above the sensor surface for ischemia monitoring in the mucosal tissue layer of the intestinal tract.

As shown in Fig. 4(a), each electrode is $y = 1.2$ mm long and $x_3 = 300$ μm wide. Between current injecting (A, D) and voltage measuring electrodes (B, C), the distance (between A and B and between C and D) is $x_2 = 150$ μm and the distance between the inner voltage measuring electrodes (between B and C) is $x_1 = 500$ μm.

The sensor was manufactured using a commercial standardized PCB processes with an electrodeposited soft pure (99.9%) gold finish (10–15 μm copper, with 3—5 μm nickel, and 1-μm pure soft gold) and a rigid 1.55-mm-thick FR-4 substrate by P.W. Circuits (Leicester, U.K.), as shown in Fig. 4(a).

A. Bipolar Saline Solution Measurements

The sensor was characterized using saline solutions. First bipolar impedance measurements were performed to measure each electrode impedance versus a stainless-steel AISI304L (Fe/Cr18/Ni10) temper annealed electrode (Advent Research Materials, catalog number FE692411), with a thickness of 50 μm and 50 mm $\times$ 50 mm in size, with both sides of the electrode in contact with the solution [Fig. 4(b)]. These measurements were obtained without the front-end amplifier but by using the 16047E fixture. The stainless-steel electrode is significantly larger than the electrodes of the sensor of Fig. 4(a), such that its interfacial impedance may be considered negligible. Consequently, a two-point measurement is sufficient to establish the impedance of each of the sensor's electrodes. A similar approach has been followed in [37]–[39].

The setup was calibrated following the built-in open/short calibration process using the 16047E fixture, either not connecting anything to the two fixture terminals (open) or shorting them together with the metal connector provided with the fixture. All measurements were performed using

Fig. 3. (a) Gain and (b) phase versus frequency responses of all the examined devices and topologies. (c) LTSpice simulations of the amplifier CMRR.

characterized using the impedance analyzer and the front-end amplifier. This electrode arrangement has been optimized using electric field finite-element method (FEM) simulations to maximize the integrated sensitivity to impedance changes

50-mV excitation (measurements with smaller amplitudes provided the same results, confirming it did not affect electrode impedances), collecting 400 points logarithmically, spaced between 20 Hz and 1 MHz. Measurements were performed with the measurement time option in the instrument set to selection 5, which, according to the manufacturer, leads to the longest measurement time and the highest measurement precision possible with the E4990A. Three measurements for trace averaging were used. Open/short calibration measurements were also performed, with point averaging, using again three measurements for greater precision. Prior to collecting the measurements, repeated fast measurements without any averaging were performed, until the electrode spectra were stable and consistent.

A 3-D printed electrode holder that fits over a 100 mL (diameter: 48 mm and height: 80 mm) translucent borosilicate glass beaker was designed to ensure a constant distance between the stainless-steel electrode and the tetrapolar sensor electrodes. In this way, the cell constant [1] of the electrochemical cell remains the same. The experimental setup is presented in Fig. 4(b), showing the impedance analyzer, the fixture, the wire connections to the electrodes, the glass beaker, and the 3-D-printed holder with the electrodes. Fig. 4(c) portrays a 3-D rendering of the 3-D-printed electrode holder, illustrating in more detail the experimental setting. The sensors are held in place in this fixture with a secondary 3-D-printed fixture, which also protects the electrical connectors from the solutions. The main fixture was printed by a Fortus 400 mc using a biocompatible material (ABS-M30i) and the secondary fixture was printed by a Connex3 Object500 using the VeroClear material, all by Stratasys, Ltd., MN, USA.

Deionized water with a conductivity of 0.055 μS was obtained from a Veolia Elga Purelab Chorus 1 through a Halo flexible dispenser. The conductivity of the deionized water was also measured with an HANNA HI 991391 meter with an HI 1288 probe giving a conductivity, σ, of 0 mS/cm. A phosphate-buffered saline solution was then obtained by dissolving one P4417 tablet, purchased from Sigma-Aldrich, in every 200 mL of deionized water. The solution conductivity was equal to 15.24 mS/cm at a solution temperature of 19.2 °C.

Averaged measured results from eight sensors with four electrodes each (i.e., average results from 32 electrodes) are shown in Fig. 5. The error bars were computed by subtracting or adding the standard deviation of the measurements at each frequency from the average data at each frequency. The absolute maximum magnitude and phase (as a worst-case scenario) are also shown in the plots. This data were used to fit the equivalent circuit models of Fig. 5(c) and (d) using the software of [40]. The fitting results are also shown in Fig. 5(a) and (b).

Bipolar impedance measurements between different sensor electrode pairs [A–D, B–C, A–B, and C–D, see Fig. 4(a)] were also performed using the 3-D-printed fixture of Fig. 4(b) and (c) without the stainless-steel electrode. Measurements at high frequencies, where R_S dominates, are shown in Fig. 5(e). These measurements allowed an approximation of Z_{IE} [see Fig. 6(g)] together with data from Fig. 10 and data from the literature [22].
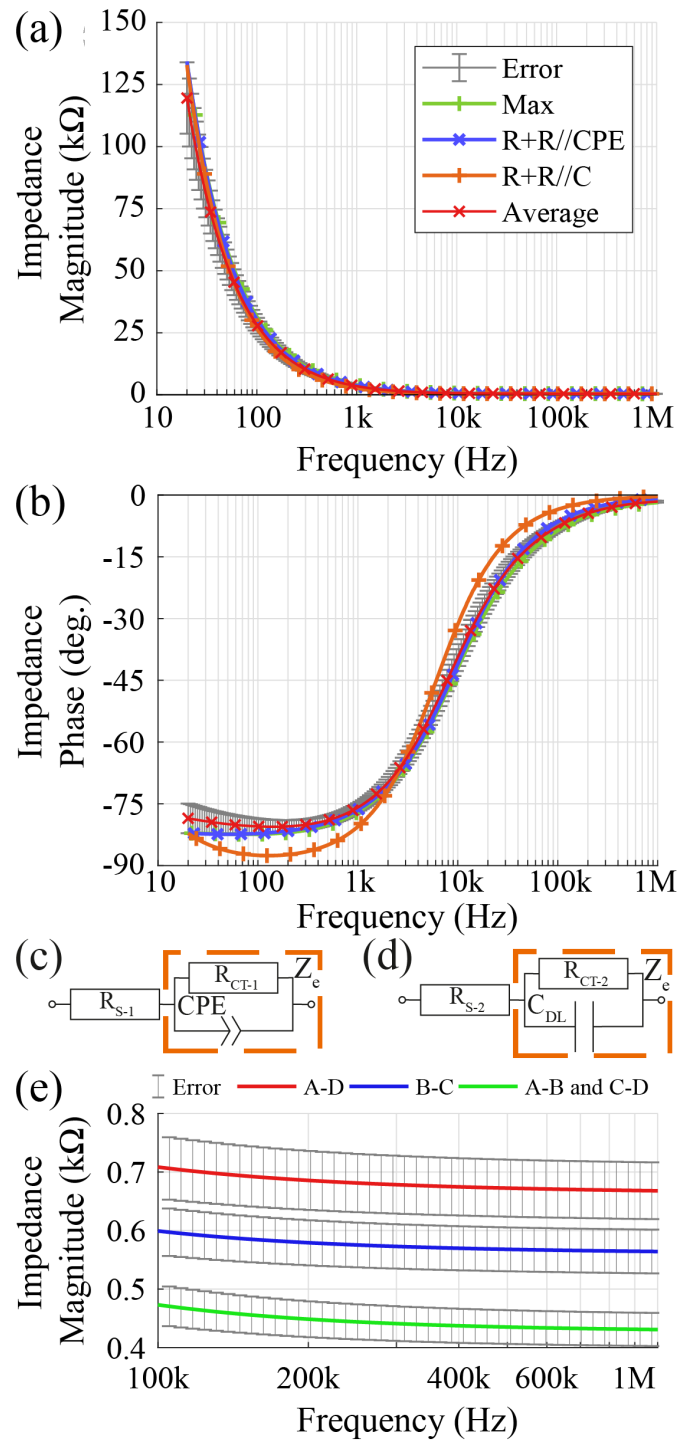

Fig. 5.   Electrode impedance versus stainless-steel electrode. (a) Magnitude and (b) phase. (c) Equivalent circuit with CPE (Model 1) and (d) with C_{DL} (Model 2). (e) High frequency bipolar impedance between different sensor electrode pairs [see Fig. 4(a)].

B. Comparison of the Derived Electrode Equivalent Circuit Model With Others From the Literature

A vast number of electrode models can be found in the literature. Some examples include the simple *RC* model of Fig. 6(a) used in [18] for up to 10 MHz (Model 3), the model of Fig. 6(b) used in [22] for up to 1 MHz, which models an electrode contact impedance, followed by the stratum corneum impedance (Model 4), the model of Fig. 6(c) proposed in [41]
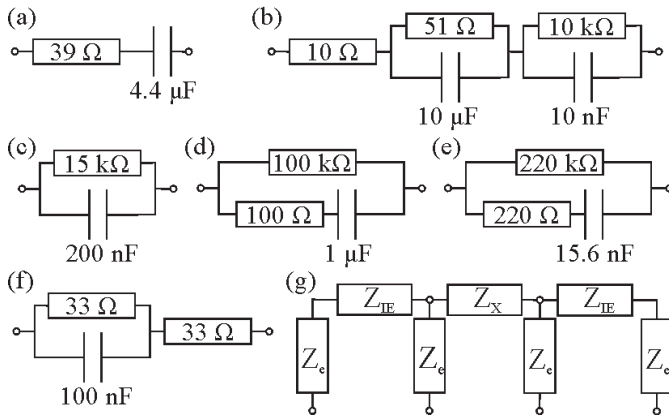
Fig. 6. Electrode models. (a) Model 3 [18]. (b) Model 4 [22]. (c) Model 5 [41], [42]. (d) Model 6 [10]. (e) Model 7 [10]. (f) Tissue model used as Z_x in [22]. (g) Between current injecting and voltage measuring electrodes there is an interelectrode impedance (Z_{IE}).

and [42] modeling the impedance of 500 μm $\times$ 200 μm platinum electrode for epidural stimulation of paralyzed rats for up to 10 kHz (Model 5), and the model of Fig. 6(d) of platinum black needles of 4 mm length and 0.5 mm diameter (Model 6) and that of Fig. 6(e) modeling high impedance electrocardiogram (ECG) electrodes (Model 7), proposed in [10] for up to 1 MHz. Attention should be paid when generating equivalent circuits for electrode interfaces, as these should model sufficiently the interface electrical properties within the BW of interest and not in just one frequency. Models 3, 4, 6, and 7 have been used for front-end characterization in the literature. As discussed in [24], the electrode interface impedance can lead to voltage loading effects and thus to measurement errors, if the differential input impedance of the amplifier is low. Consequently, to properly evaluate the examined amplifiers and to cover a wide range of applications, an electrode model that will represent a challenging (i.e., a high electrode impedance) and realistic case is required. The impedances of the electrode models of Figs. 5 and 6 were simulated with the software of [40] and are compared in Fig. 7. This was necessary to investigate how the electrode impedance and model were characterized and presented in Fig. 5 compared with other models in the literature.

IV. TETRAPOLAR MEASUREMENTS OF KNOWN LOADS IN THE PRESENCE OF THE DERIVED ELECTRODE IMPEDANCE MODELS

Following the above analysis, the amplifiers are assessed in terms of their ability to perform tetrapolar measurements of resistive loads (Z_x) with the Keysight E4990A impedance analyzer. This is done in the presence of the derived electrode interfacial impedance model (Z_e) in the absence of the solution resistance (R_{S-2}) between 20 Hz and 1 MHz. The electrode equivalent circuits and Z_x are arranged, as shown in Fig. 6(g). An illustration of the measurement setup for tetrapolar measurements is shown in Fig. 8. The aim of these experiments is to evaluate and compare all the amplifiers using the same well-controlled experimental conditions with a wide range of Z_xs that can cover a wide range of bioimpedance applications and in the presence of a challenging (high impedance) electrode model.
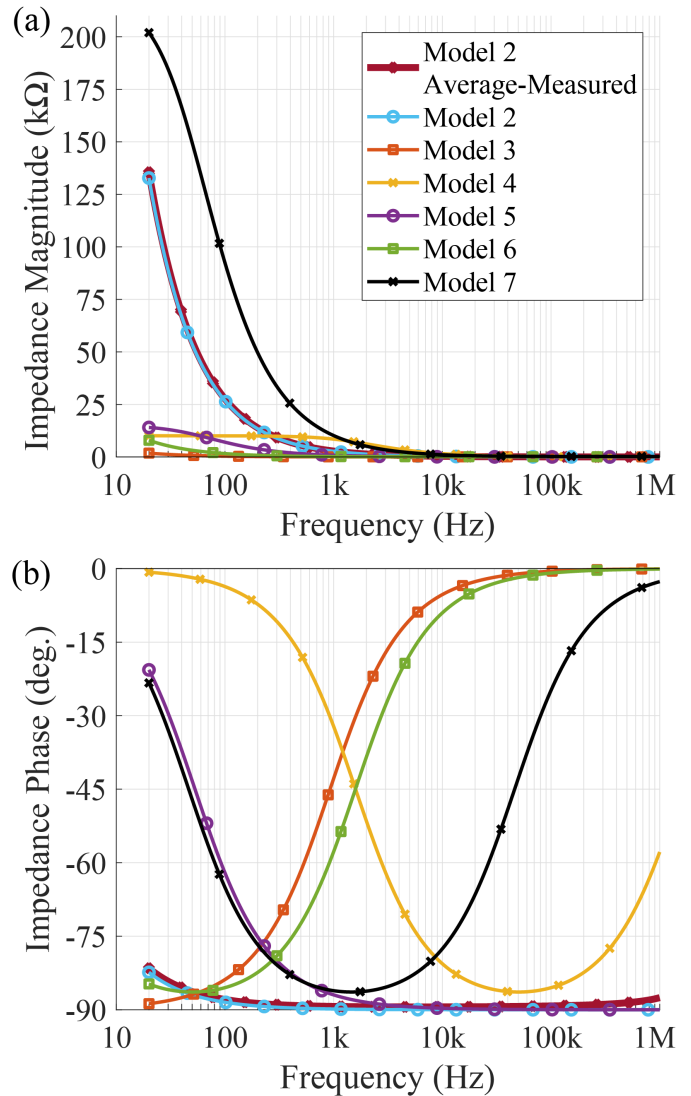

Fig. 7. Impedance (a) magnitude and (b) phase Bode plots of Models 2–7.

To keep parasitics in the experimental setup small and equal, when evaluating different amplifiers, the same coaxial leads were used to interface the amplifiers to the instrument. These were kept short and equal to 5 cm (Fig. 8). The shields of the leads were connected at the instrument side to that of each terminal and on the measurement side they were sorted together as in the 4TP configuration [19]. Due to being short, the coaxial cables were not very flexible, and no mechanical motions were allowed during measurements that could have introduced a varying parasitic.

All tetrapolar measurements were performed using the Wenner/Schlumberger injection/measurement electrode arrangement [8], where the outer pair of electrodes (A and D) is used to inject current and the inner pair (B and C) is used to measure the resulting voltage [see Fig. 4(a)]. The electrode model ($Z_e = R_{CT-2}//C_{DL} = 1$ MΩ//60 nF) of Fig. 5(d) was used to build the four Z_e of Figs. 1(b) and 6(g), as shown in Fig. 8. Strip wiring boards and 5% tolerance through-hole components were used to allow parasitics and electrode model mismatches and, thus, closer mimic a realistic scenario. These were then measured using the E4990A impedance analyzer
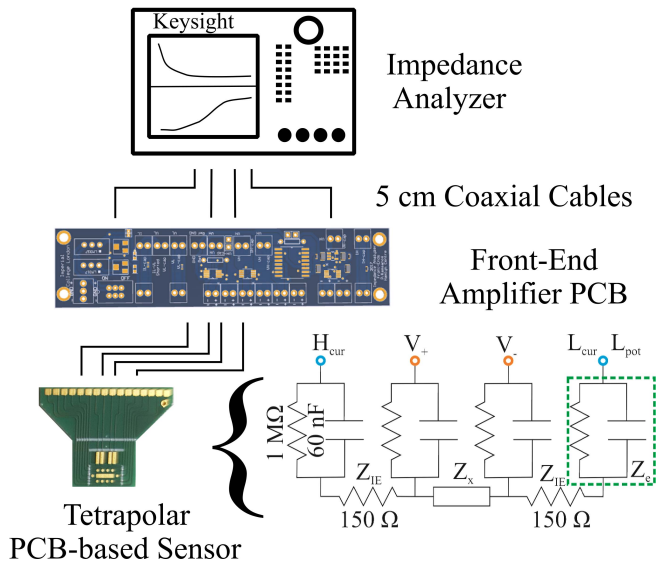
Fig. 8. Experimental set-up for tetrapolar impedance measurements. The impedance analyzer is connected with 5-cm-long coaxial cables to the amplifier and then this connects to either the four electrodes of the tetrapolar sensor of Fig. 4(a) or to the RC electrode equivalent circuits of each electrode of this sensor and the load under measurement (Z_x). The 3-D-printed electrode support of Fig. 4(c) was used for saline solution measurements. The orange nodes connect to the amplifier inputs and the blue nodes to the impedance analyzer via the PCB. The sensor's electrodes B and C [see Fig. 4(a)] connect to the amplifier inputs, while electrodes A and D to the analyzer.

and the 16047E fixture using three measurements for trace averaging, and the same calibration files, as discussed previously, for electrode characterization. The measured results from the four Z_e were then averaged all together and the results are shown in Fig. 7, where they are compared with the simulated ones.

As shown in Fig. 6(g) and discussed in [22], in reality due to the separation between electrodes A and B and between electrodes C and D, there is a small impedance between these electrode pairs, Z_{IE}. For reasons discussed in Section VI, in this article, Z_{IE} was set to 150 Ω. In cases where the volume conductor changes isotropically, as in the saline solution measurements of Fig. 10, when the impedance under study changes, so will Z_{IE}. However, in cases where the volume conductor being measured changes anisotropically, Z_{IE} can be constant. For example, the volume being monitored can be centered and confined within the B–C electrode spacing. In this study, it will be kept constant for simplicity and only Z_x will vary. The use of Z_{IE} is not critical and others often exclude it [10], [18], [24], [30]; however, its use as in [22] leads to a more realistic and challenging scenario, as the total load seen in the current path is increased, leading to a smaller voltage swing across Z_x. Having built the model of Fig. 6(g), as shown in Fig. 8, this was then used to measure a range of Z_xs.

Resistive loads from 10 Ω to 100 kΩ (10 Ω, 24 Ω, 40 Ω, 51 Ω, 100 Ω, 242 Ω, 510 Ω, 1 kΩ, 2.2 kΩ, 5.1 kΩ, 10 kΩ, 51 kΩ, and 100 kΩ) were used as Z_x in the circuit of Fig. 6(g). The model used in [22] to model deep viable tissue, shown in Fig. 6(f), was also built and used. As can be seen, tissue is modeled with a reactive component. This diminishes with increasing frequency, leading to a smaller impedance. In the

circuit of Fig. 6(f), the impedance is 66 Ω at DC and decreases to 33 Ω at 10 MHz. Consequently, using fixed resistors of large values constitutes a stricter test for the evaluation of the amplifiers, while using a wide range of resistive loads (up to 100 kΩ) covers an extensive range of potential applications. For example, these values fall within the range of reported impedances of ischemic tissues, which can range from a few hundreds of ohms [5] to 5 kΩ [6] or even approaching 10 kΩ [7]. These loads were all measured using the E4990A and the 16047E fixture for two-point measurements, with trace averaging using three measurements, to provide reference measurements for comparison. The measurements were calibrated as before using the open/short calibration process. Commercially available through-hole resistors were used to realize these loads for ease. In contrast to surface-mounted metal film resistors, these have a poor frequency response. At 1 MHz, where the greatest deviation takes place, the 100-kΩ resistor was measured to be 97 kΩ (3.7% change in value) with a $-9°$ phase, the 51 kΩ, 50.7 kΩ (0.75%) with $-3.7°$ phase, while for loads below 10 kΩ, the magnitude deviation was below 0.18% with a phase of less than $-1°$. Consequently, the use of through-hole resistors was not an issue, as the load values, particularly from 10 kΩ and below, did not change significantly.

Tetrapolar measurements of the loads in the presence of Model 2 and Z_{IE} [Fig. 6(g)], with the front-end amplifiers and without any calibration, were then performed to compare the amplifiers. The calibration method mentioned earlier, as discussed in the introduction, is valid only for two-point measurements. As before, three measurements for trace averaging via the instrument were used. Details with regard to the measurement uncertainty of the instrument can be found in its data sheet. The measurement deviations compared with reference measurements of the loads directly through the impedance analyzer are shown in Fig. 9. Phase measurement error was calculated as the difference between the two measurements and magnitude error was calculated as the difference divided by the reference measurement. Fig. 9(a) shows the magnitude and phase measurement errors in the measurement of the tissue equivalent circuit of Fig. 6(f) as a function of frequency. The magnitude measurement error for INA111 is not shown in its entirety for clarity, but at 20 Hz, it goes down to -654.5% and at 1 MHz to -203%. Fig. 9(b) and (c) shows the measurement errors in the measurement of different examined resistive loads at 20 Hz and 1 MHz, respectively. The INA111 magnitude error at 20 Hz goes down to -1900% for a 24-Ω load and down to -4580% for the 10-Ω load. These are not shown for clarity. Table III tabulates the results at 20 Hz and 1 MHz for loads of 10 Ω and 10 kΩ (i.e., the range of interest for our application) extracted from the trace-averaged plots of Fig. 9(b) and (c).

V. TETRAPOLAR SOLUTION MEASUREMENTS

Tetrapolar measurements were then performed using the AD8066/AD8130 front-end, the E4990A impedance analyzer, the sensor of Fig. 4(a), and solutions of conductivities equal to 0.05, 2.5, 5, 7.5, 10, 12.5, 15, 17.5, and 20 mS/cm.
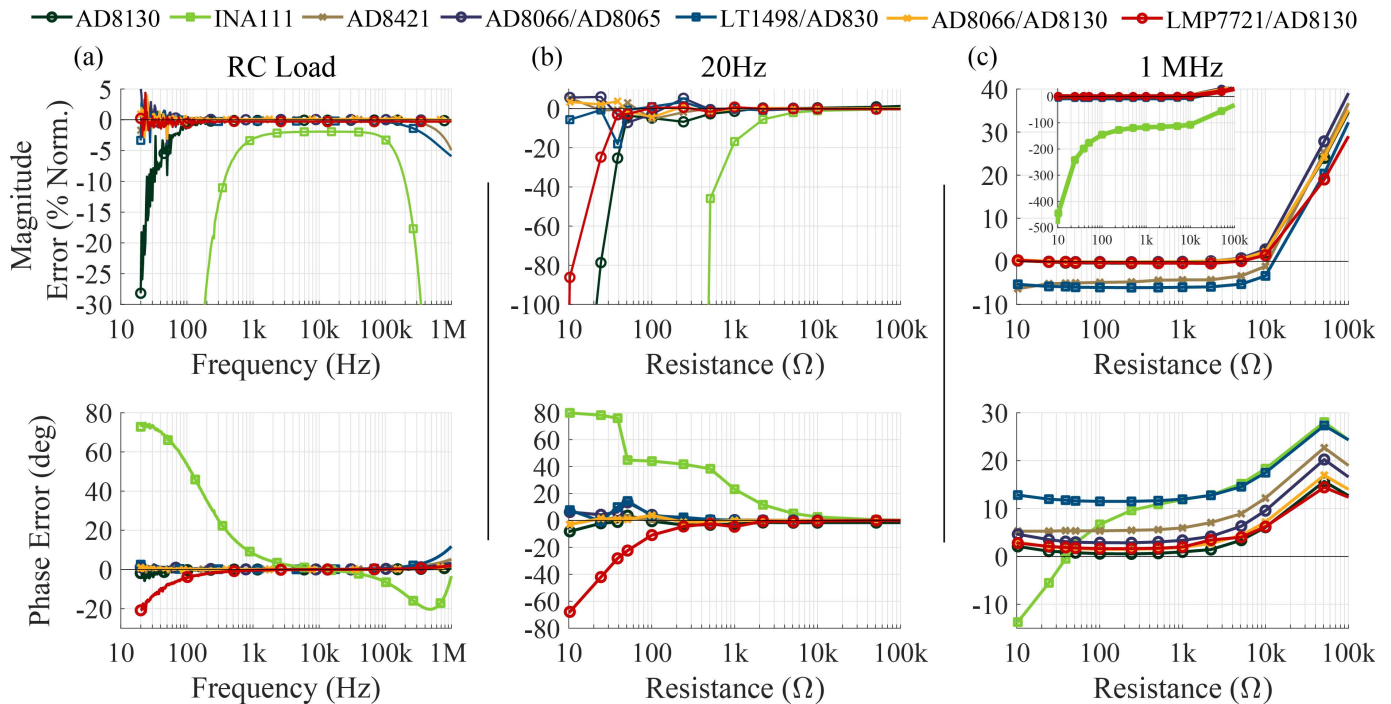
Fig. 9. Measurement error in the measurement of different loads in the presence of the electrode contact impedances. (a) Error in the measurement of the *RC* load of Fig. 6(f). Measurement error of different test resistors at (b) 20 Hz and (c) 1 MHz. The inset in (c) also shows the error for INA111.

TABLE III
MEASUREMENT ERRORS AT 20 Hz AND 1 MHz (ABSOLUTE ROUNDED VALUES)

Freq (Hz)	R (Ω)	INA111		AD8130		AD8421		LT1496/AD830		AD8065/AD8066		LMP7721/AD8130		AD8066/AD8130	
		Mag (%)	Ph (deg)	Mag (%)	Ph (deg)	Mag (%)	Ph (deg)	Mag (%)	Ph (deg)	Mag (%)	Ph (deg)	Mag (%)	Ph (deg)	Mag (%)	Ph (deg)
20	10	4,580	80	229	8.1	5.5	3	5.7	7	5.7	6.3	86.2	67.8	**3.4**	**2.8**
	10 k	1.1	2.6	0.4	1.6	**10e-3**	0	0.3	**0**	0	0	0.1	0.4	0.1	**0**
1 M	10	445	13.7	0.2	2.1	6.3	5.3	5.3	12.8	**0.2**	4.6	0.25	**2.8**	0.35	3
	10 k	108	18.3	2.2	6.1	**1.2**	12	3.4	17.5	3	10	1.4	**6.2**	2.25	7

Details with regards to the measurement uncertainty of the instrument can be found at the impedance analyzer data sheet.

The 3-D-printed fixture and beaker shown in Fig. 4(b) and (c) were used for these measurements, without the stainless-steel electrode. As before, a 50-mV excitation was used as well as three measurements for trace averaging. No calibration was used. The measured results are shown in Fig. 10. As it can be seen from Fig. 10(a), these solution conductivities led to loads varying between 150 Ω and 1.3 kΩ, approximately, which are within the range of interest for bioimpedance measurements. Impedance magnitude measurements at intermediate frequencies (25–750 kHz), obtained by extracting data from Fig. 10(a), where errors due to the instrumentation are minimal, were used to obtain the plot of Fig. 10(c). The data were obtained by computing the average measured solution impedance magnitude at 100 Hz, 250 Hz, 500 Hz, 750 Hz, 1 kHz, 2.5 kHz, 5 kHz, 7.5 kHz, 10 kHz, 25 kHz, 50 kHz, 75 kHz, 100 kHz, 250 kHz, 500 kHz, and 750 kHz versus solution resistivity, ρ ($\rho = 1/\sigma$). The error bars based on the standard deviation of the measurements are included in Fig. 10(c). The data were fitted using a linear trendline providing an $R^2 = 0.9998$. These measurements are a practical example for the use of the amplifier, demonstrating how it can be used to characterize

a tetrapolar sensor and the measurement of the sensor's cell constant.

VI. DISCUSSION

As it can be seen from Fig. 3, although INA111 provides FET inputs and thus a high input impedance and low input bias current (Table I), its use above 50 kHz can be problematic. This is due to large phase shifts and gain peaking. Furthermore, its CMRR is the smallest at high frequencies [Fig. 3(c)]. The AD8421 provides a higher BW than INA111. It also provides a low input bias current and a high input impedance when compared with the AD8130 (Table I). However, its CMRR drops significantly at high frequencies [Table I and Fig. 3(c)], while it introduces large phase shifts [Fig. 3(b)], as well as some gain peaking in its passband [Fig. 3(a)]. The AD8065 appears to outperform INA111 (Table I). Having FET inputs also provides a very high input impedance.

Recognizing the advantages and disadvantages (low input impedance and a relatively high input bias current, possibly due to a bipolar input stage) of the AD830 (see Table I), the use of the AD843 was proposed in [10] to buffer its
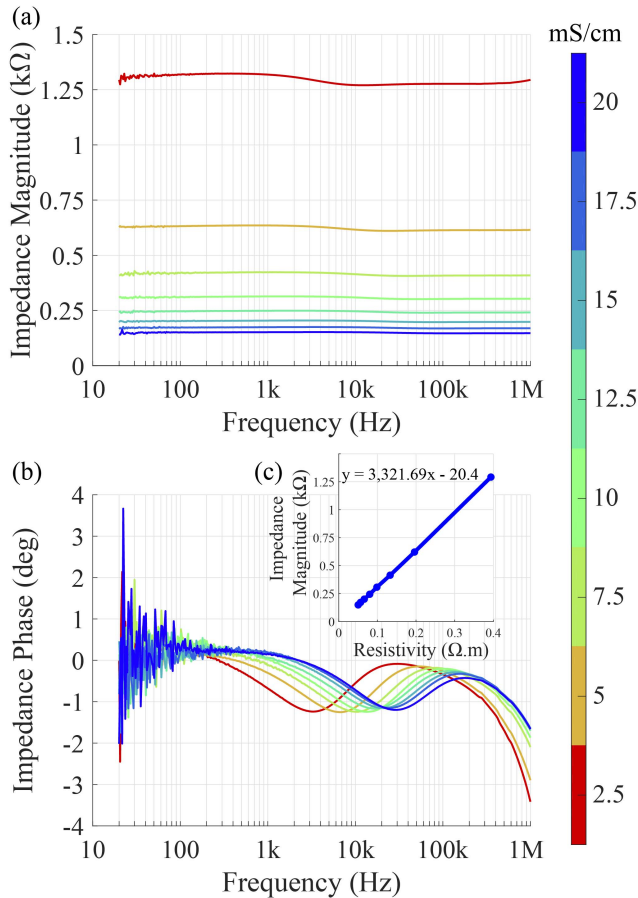
Fig. 10. Tetrapolar impedance (a) magnitude and (b) phase measurements from solutions of different conductivities. (c) Measured impedance magnitude as a function of resistivity.

inputs and provide a higher input impedance (Table II). The LT1498 was proposed in [4] to buffer the inputs of the AD830. This, however, reduces the overall BW, while it also increases the input bias current (as it is a bipolar transistor amplifier) and thus reduces the input impedance of the topology (Table II), in comparison to the AD843. It also provides the second worst phase response after INA111 [Fig. 3(b)]. The LT1498/AD830 phase goes down to −140° and the AD8421 to −180° at 10 MHz, while the INA 111 exceeds these. These are not shown for clarity. The MAX435 is a discontinued product and has been included in Table I for completeness. Suffering also from low input impedance, it was combined with the EL2244. This IA was reported in [10] to have a 60 MHz, −3 dB BW and a CMRR at low frequencies of 85 and 76 dB at 1 MHz and 56 dB at 10 MHz. The disadvantage of the AD8066/AD8065 topology based on the standard three op-amp IA is that good resistor matching is required in the differential stage for a high CMRR. This is not the case with topologies using a DDA. To address this, 1 kΩ, 0.01% resistors were used for the realization of the circuit of Fig. 2(b). This amplifier comes with the disadvantage of a higher cost and an overall larger PCB design, primarily due to the high accuracy resistors. These resistor tolerances were used to simulate the effect of resistor mismatches to the circuit's CMRR. As shown in Fig. 3(c), a CMRR between 140 and 74 dB can be achieved. This is a significant spread.

Although both the AD830 and AD8130 are DDAs, with similar CMRR characteristics [Fig. 3(c)], among other parameters which are also improved, the AD8130 has a wider BW and a higher input impedance, as shown in Table I. The AD8130 provides the widest BW and lowest phase delay [Fig. 1(a) and (b)], as well as a high CMRR at high frequencies (Table I). However, the AD8130 provides a relatively low-input impedance and a high input bias current, possibly due to a bipolar input stage. Consequently, apart from these shortcomings (which constitute a major disadvantage), the AD8130 provides the best performance. To improve the input impedance, it can be buffered with the AD8066, which is a dual version of AD8065 with identical characteristics. Alternatively, the CMOS input stage LMP7721 can be used, which has the smallest input bias current among the components discussed in this article (Table II) and a rail-to-rail output.

According to the results of Fig. 3, the best performance in terms of gain flatness and phase is obtained with the front-ends employing the AD8130. All three amplifiers have a gain of 0 dB at 1 MHz, with the phase of the AD8066-buffered version achieving a marginally decreased phase response at 10 MHz of −14° versus −5°, when compared with the unbuffered AD8130, attaining, however, a higher input impedance (see Tables I and II). When using the LMP7721, the 10-MHz phase goes down to −20°. Since the CMRR depends on the differential stage, the DDA-based amplifiers all have identical CMRR, with a value of 100 dB at DC and up to 12 kHz, reducing to 73 dB at 1 MHz and 54 dB at 10 MHz [Fig. 3(c)]. In the vast majority of bioimpedance applications [13], measurements up to 1 MHz are sufficient; thus, the rest of this article focuses on the performance of the amplifiers within this BW.

To measure impedance, the phase of the recorded voltage signal with regard to the injected signal to the SUT is important. Impedance can be represented as a magnitude and phase or as real and imaginary components. If the recording amplifier introduces phase delay to the recorded signal, the impedance analyzer will see this delay as part of the phase of the load. This is also important when using custom instrumentation with either analog or digital impedance computation. For example, common computation in the analog domain of the real and imaginary components is performed using synchronous detection, also known as phase-sensitive detection [1], [13]. Such delays will affect the computation of both the real and imaginary components. This will also influence the phase measurement of magnitude/phase measurement systems [12], [14]. Phase delays in the measurement system thus need to be known, as they will affect impedance measurement [13], [43] and must be compensated for (e.g., using the methods of [43]). Consequently, the AD8066/AD8130 front-end presents a useful solution for the front-end amplifier of bioimpedance instrumentation systems based on discrete components.

The measurement of the electrode impedances of the PCB-based tetrapolar impedance sensor is presented in Fig. 5. The average value for the impedance magnitude [Fig. 5(a)] is the highest at 20 Hz, as expected, reaching ∼120 kΩ ± 14 kΩ. At 1 MHz, this is reduced to ∼420 Ω ± 20 Ω. The average phase [Fig. 5(b)] varies from −78.5° ± 3.6° to −1.6° ± 0.25° at 1 MHz. Using the maximum absolute values

to obtain an equivalent model of the electrode impedance provides a realistic worst-case scenario for the testing of the front-ends [24].

In the equivalent circuits of Fig. 5, R_S models the solution resistance, which dominates at high frequencies, and R_{CT}, the charge transfer resistance, while a capacitive element models the interfacial double layer capacitance. The latter is performed in Fig. 5(d) by a capacitor, C_{DL}, and in Fig. 5(c) with a constant phase element (CPE), which is essentially the model of an imperfect capacitor (Model 1). The impedance of a CPE is given by $Z_{CPE}(\omega) = Q^{-1}(j\omega)^{-n}$, where Q is referred to as the CPE parameter, which has no real physical meaning and its units are $S.s^n$ and n is referred to as the CPE exponent. When $n = 1$, the CPE acts as a perfect capacitor, with a 90° phase shift and when $n = 0$, the CPE acts as a resistor producing a 0° phase shift. Thus, depending on n, the phase delay of the element is constant with a value of $-90° \times n$. It is well known that electrode impedance can be modeled well using a CPE in the model. However, a CPE can be approximated with real components using complex RC ladder networks, which are not trivial to build [44]. In order to build a simple equivalent RC network to be used for evaluating the front-end amplifiers, the circuit of Fig. 5(d) can be used instead (Model 2). Within the context of this work, a good fit of the impedance magnitude is required, while the phase is not as important. What is important is the comparison of the electrode impedance with the differential input impedance of the amplifier, as this will establish the measurement error due to loading effects [24], while the phase is not relevant. This is discussed in more detail in the introduction [discussion around (1)]. The component values fitted to the data that correspond to the circuit of Fig. 5(c) were set equal to $R_{S-1} = 439$ Ω, $R_{CT-1} = 8$ MΩ, $Q_{CPE} = 85$ nS·s^n, and $n = 0.925$ and for the circuit of Fig. 5(d) $R_{S-2} = 439$ Ω, $R_{CT-2} = 1$ MΩ, and $C_{DL} = 59.4$ nF. Indeed, Model 1 is a better model providing a closer fit to the experimental data. This is particularly true for the phase, as opposed to Model 2. Nevertheless, the proposed RC equivalent circuit [Fig. 5(d)] models sufficiently well the electrode impedance magnitude for the purpose of this study, which is the factor of interest that may hinder front-end measurements at low frequencies [24]. At 20 Hz, the model achieves a 133-kΩ impedance, when the maximum value from the average experimental data was 135 kΩ (1.5% error), and at 1 MHz, the measurements are approximately the same. It achieves a maximum normalized percentage error of 34.5% at 3 kHz, having a value of 990 Ω instead of 1.5 kΩ, while the CPE-based model achieves a maximum error of 7% at 12.5 kHz.

The measurements and simulations in Fig. 7 of the electrode models of Fig. 5(d) (without R_{S-2}) and Fig. 6(a)–(e) demonstrate the varying characteristics of different electrodes. When compared with other models used to evaluate front-end amplifiers, the impedance of the examined electrodes has the second highest impedance, with the vast majority having significantly smaller impedance at 20 Hz (Fig. 7). Consequently, this is a good and challenging electrode and model for the evaluation of the front-end amplifiers with regard to their finite input impedance [see (1)] [24]. For example, if the

electrode impedance is very low, then all amplifiers would perform well at low frequencies and it would thus be hard to evaluate them properly. In applications with higher electrode impedances, the weakest amplifier will continue to behave the worst, while the best will demonstrate superior performance. Consequently, the use of this high impedance electrode model allows the overall conclusions and analysis to be translatable and used as a guide for other cases. To implement the model with real components, we have used $R_{CT-2} = 1$ MΩ and $C_{DL} = 60$ nF. The measured Z_e RC model follows well the simulated one, with a maximum normalized deviation of 8.6% in magnitude and 2.5° phase deviation at 1 MHz and 2% and 0.8° deviations at 20 Hz, which arise due to through-hole component and strip board parasitics.

Different electrode separations lead to different measured solution resistances and the further away they are, the largest R_S should be. This is defined by the cell constant of an electrode arrangement, which depends on the separation between electrodes, their geometry, and arrangement [45]. The further away they are, the larger is the cell constant and the greater the solution volume probed by a pair of electrodes. Consequently, different electrode pairs will measure a different R_S at high frequencies. This is evident from Fig. 5(e). With electrodes A and D being the furthest apart, the impedance measured at high frequencies is the greatest (670 Ω ± 48 Ω). This is followed by the impedance measured between electrodes B and C (565 Ω ± 37 Ω), while the impedance between electrodes A and B and between electrodes C and D is the smallest (430 Ω ± 28 Ω), as these are the closest spaced electrode pairs [see Fig. 4(a)].

These results are also important for the design of custom instrumentation. For example, knowledge of the high frequency A–D impedance is vital for the ac current source design and its output impedance, while the B–C impedance is important for the gain requirements of the voltage front-end. The fact that the high-frequency impedance is smaller between electrodes B and C is beneficial for the current source, while the greater potential difference between electrodes A and D is also beneficial for the voltage front-end. Given that reciprocity applies, this can be exploited to relax instrumentation requirements, although this is not performed in this article. Measurements of the impedance between electrodes A–C and B–D have been omitted, as there are no direct circuit connections between these two electrode pairs or individual elements of the circuit of Fig. 6(g).

The 15 mS/cm saline solution measurement of Fig. 10(a), which will be discussed later, is approximately the same with the conductivity of the PBS solution (15.24 mS/cm) used in the measurement of Fig. 5(e). The tetrapolar resistance measurement of the 15 mS/cm indicates that $Z_x \approx 200$ Ω. This is significantly smaller than the impedance measured between electrodes B and C (564 Ω ± 37 Ω). The measurement between electrodes A and D at high frequencies (where electrode interfacial impedance diminishes) of Fig. 5(e), according to Fig. 6(g), is equal to $2 \times Z_{IE} + Z_x = 670$ Ω ± 48 Ω and thus, in this specific case, $Z_{IE-2} = 235$ Ω. As it can be seen, the A–B and C–D impedances at high frequencies (430 Ω ± 28 Ω) cannot be used to approximate Z_{IE}, as expected. In [22], this was set to $Z_{IE-1} = 100$ Ω.

The average value of Z_{IE-1} and Z_{IE-2} is equal to 167.5 Ω. Based on component availability, Z_{IE} was roughly set to 150 Ω.

The load measurements via the front-ends and the impedance analyzer in Fig. 9 demonstrate the superiority of the AD8066/AD8130 both at low and high frequencies and in the range of the examined loads. Overall, the greatest measurement deviations were observed with INA111. As is evident from Fig. 9(a), the low input impedance of AD8130 leads to large measurement errors in the measurement of small loads at 20 Hz. Nevertheless, when used with a high input impedance buffer, this is improved. In Fig. 9(a), at 20 Hz, the smallest magnitude error was achieved with LMP7721/AD8130 (0.23%), followed by AD8066/AD8130 (1%) and AD8421 (1.7%). In terms of phase, the smallest error in Fig. 9(a) was achieved with AD8421 (0.7°), followed by AD8066/AD8130 (0.9°) and AD8066/AD8065 (1.2°). At high frequencies, the topologies using AD8130 and AD8065 outperform the rest. According to Fig. 9(b), at 20 Hz, apart from AD8130, INA111, and LMP7721/AD8130, all other front-ends achieve similar performance, with the AD8066/AD8130 performing marginally better. At 1 MHz [Fig. 9(c)], for loads up to 10 kΩ, AD8421 and LT1496/AD830 show the worst performance after INA111, while the best performance is achieved with LMP7721/AD8130, followed by AD8066/AD8130 and AD8130. However, the lower performance of AD8130 and LMP7721/AD8130 at low frequencies leads us to conclude that AD8066/AD8130 is the best front-end among the examined architectures for the particular application, examined loads and electrode model.

According to the data of Fig. 9(b) and (c), an uncalibrated worst-case measurement deviation of 4.4% in magnitude and 4° at 20 Hz was achieved with the AD8066/AD8130, while at 1 MHz, these were 2.25% and 7° with loads between 10 Ω and 10 kΩ. With loads up to 100 kΩ at 1 MHz, these increase to 35% and 17°. At low frequencies [Fig. 9(b)] and small loads, the percentage error is larger because of the large electrode impedance and the imposed error being similar to the measured load impedance. At high frequencies [Fig. 9(c)] and small loads, the error is small because the electrode impedance diminishes, and it increases as the load increases due to the larger time constant formed with the parasitic capacitances seen at the inputs of the amplifier. As it can be seen from (1), the relationship between electrode impedance, measured load, and amplifier differential input impedance is important and will dictate the measurement error. This further supports the deviations in the measurement of varying load resistance and at different frequencies, as in the case of the use of the AD8130 without input buffers.

As mentioned earlier, typically, tissue impedance can vary from a few hundreds of ohms up to 10 kΩ. Within this range of measured loads, the measurement error at 1 MHz for 10 kΩ is below 2.25% and 7° for the magnitude and phase, respectively, with the AD8066/AD8130. The above conclusions are supported by the data of Table III, where the superiority of the proposed architecture at low frequencies and loads is clear. Where other front-ends appear to perform better at higher frequencies and loads, it is only marginally, while

other amplifiers achieve significantly worse performance at low frequencies and loads. While all these numbers (Table III) are specific to the testing conditions used, as discussed earlier with regard to Fig. 7, the overall conclusions are useful to other bioimpedance applications using electrodes with higher or lower impedances. In addition, the measured loads cover a wide range of bioimpedance applications. Especially in applications where the electrode impedances (as is the case when characterizing an impedance sensor) and loads are unknown, it is important to use an amplifier that can cope with large impedances. The results presented in this article highlight which amplifier attributes need to be taken into consideration for general bioimpedance applications. Finally, the analysis presented thus far is particularly useful to establish whether an amplifier is suitable for a particular application.

Having established that the AD8066/AD8130 is the most preferable topology, it is used for the measurement of the impedance of solutions of different conductivities using the examined tetrapolar sensor. The measurements of Fig. 10 demonstrate that the measured impedance is relatively constant, as expected, due to the resistive characteristics of the saline solution. It is important to note that at low frequencies, the magnitude remains constant [as shown in Fig. 9(a)] and thus we can conclude that the amplifier is successful in measuring these conductivities in the presence of the large electrode contact impedances of the examined electrodes. The fluctuation in the phase measurement is similar to that observed in the phase plot of Fig. 9(a). We assume that this is to some extent because of noise, as due to the large electrode impedance, the voltage swing across the load being measured is limited, while high electrode impedances lead to high noise [46]–[50]. In addition, as discussed in [31], the limited CMRR will lead to a CM error signal that will add to the phase measurement error. This error signal depends on electrode impedances and their mismatches. Due to the large electrode impedances at low frequencies, these CM errors will thus be greater at these frequencies. A 50-mV signal was used in all measurements presented in this article, and a larger excitation would reduce these errors. Nevertheless, this fluctuation is within ±3.4° and is negligible. At high frequencies, the magnitude also remains constant, as expected from the BW characteristics of the amplifier (Fig. 3) and the measurements of Fig. 9. The greatest phase delay measured at 1 MHz in Fig. 10(b) was for the lowest conductivity solution and was equal to 3.3°. According to Fig. 3(b), the phase error of the amplifier is −1° at 1 MHz, while according to Fig. 9(c), the maximum phase error for loads within the range examined in Fig. 10(a) is less than 3°. In addition, there are parasitic impedances between electrodes via the FR4 substrate and additional parasitics due to the interconnections between the sensor and the amplifier that will contribute to the phase being measured. These explain the small phase delay recorded and the small change in the magnitude with increasing frequency. The measurement of solutions of known conductivities allows the characterization of the examined sensor. The slope of the curve of Fig. 10(c) enables the estimation of the cell constant of the sensor, which is equal to the slope (3321.7 m^{-1}).

VII. Conclusion

Commercial bench-top impedance analyzers represent the gold standard and provide a reference point for accurate impedance measurements. Such instruments are essential in characterizing material and device impedances and sensors. For example, they are necessary to verify experimentally the design of impedance sensors or to obtain the expected impedance range of a targeted load to provide design specifications for the development of custom miniature electronics. However, many impedance analyzers are incapable of performing tetrapolar impedance measurements in applications where there are large contact impedances, such as in the field of bioimpedance. Published and new front-end topologies proposed to enhance and expand their operation and use in such applications were examined. When comparing measurements of resistive loads in the presence of electrode interfacial impedance models, the proposed AD8066/AD8130 front-end amplifier demonstrated the best performance at low frequencies (20 Hz), where electrode contact impedance is large, with an impedance magnitude and phase error of 3.4% and 2.8°, respectively. This was then used to characterize a tetrapolar sensor in saline solutions. The examined and proposed front-end amplifiers are applicable to any impedance analyzer and LCR meter, while they can also be used for impedance measurements with custom electronics without the use of an impedance analyzer. The results and methods presented can thus be used as a guide for choosing the appropriate front-end amplifier for such applications and for the characterization of custom bioimpedance instrumentation.

Acknowledgment

References

[1] P. Kassanos, H. M. D. Ip, and G.-Z. Yang, "A tetrapolar bio-impedance sensing system for gastrointestinal tract monitoring," in *Proc. IEEE 12th Int. Conf. Wearable Implant. Body Sensor Netw. (BSN)*, Jun. 2015, pp. 1–6, doi: 10.1109/BSN.2015.7299403.

[2] P. Kassanos, S. Anastasova, and G.-Z. Yang, "Electrical and Physical Sensors for Biomedical Implants," in *Implantable Sensors and Systems: From Theory to Practice*. Cambridge, U.K.: Springer, 2018, pp. 99–195.

[3] D. K. Stiles and B. A. Oakley, "Four-point electrode measurement of impedance in the vicinity of bovine aorta for quasi-static frequencies," *Bioelectromagnetics*, vol. 26, no. 1, pp. 54–58, Jan. 2005, doi: 10.1002/bem.20074.

[4] M. Rahal, J. M. Khor, A. Demosthenous, A. Tizzard, and R. Bayford, "A comparison study of electrodes for neonate electrical impedance tomography," *Physiol. Meas.*, vol. 30, no. 6, pp. 73–84, Jun. 2009, doi: 10.1088/0967-3334/30/6/S05.

[5] O. Casas *et al.*, "*In vivo* and *in situ* ischemic tissue characterization using electrical impedance spectroscopya," *Ann. New York Acad. Sci.*, vol. 873, no. 1 ELECTRICAL BI, pp. 51–58, Apr. 1999, doi: 10.1111/j.1749-6632.1999.tb09448.x.

[6] M. Tijero *et al.*, "SU-8 microprobe with microelectrodes for monitoring electrical impedance in living tissues," *Biosensors Bioelectron.*, vol. 24, no. 8, pp. 2410–2416, Apr. 2009, doi: 10.1016/j.bios.2008.12.019.

[7] R. Gómez *et al.*, "A SiC microdevice for the minimally invasive monitoring of ischemia in living tissues," *Biomed. Microdevices*, vol. 8, no. 1, pp. 43–49, Mar. 2006, doi: 10.1007/s10544-006-6381-y.

[8] P. Kassanos, A. Demosthenous, and R. H. Bayford, "Comparison of tetrapolar injection-measurement techniques for coplanar affinity-based impedimetric immunosensors," in *Proc. IEEE Biomed. Circuits Syst. Conf.*, Nov. 2008, pp. 317–320, doi: 10.1109/BIOCAS.2008.4696938.

[9] P. Linderholm, T. Braschler, J. Vannod, Y. Barrandon, M. Brouard, and P. Renaud, "Two-dimensional impedance imaging of cell migration and epithelial stratification," *Lab Chip*, vol. 6, no. 9, pp. 1155–1162, 2006, doi: 10.1039/B603856E.

[10] D. Yelamos, O. Casas, R. Bragos, and J. Rosell, "Improvement of a front end for bioimpedance spectroscopya," *Ann. New York Acad. Sci.*, vol. 873, no. 1, pp. 306–312, Apr. 1999, doi: 10.1111/j.1749-6632.1999.tb09478.x.

[11] B. Fu and T. J. Freeborn, "Residual impedance effect on emulated bioimpedance measurements using keysight E4990A precision impedance analyzer," *Measurement*, vol. 134, pp. 468–479, Feb. 2019, doi: 10.1016/j.measurement.2018.10.080.

[12] P. Kassanos, I. F. Triantis, and A. Demosthenous, "A CMOS magnitude/phase measurement chip for impedance spectroscopy," *IEEE Sensors J.*, vol. 13, no. 6, pp. 2229–2236, Jun. 2013, doi: 10.1109/JSEN.2013.2251628.

[13] P. Kassanos, L. Constantinou, I. F. Triantis, and A. Demosthenous, "An integrated analog readout for multi-frequency bioimpedance measurements," *IEEE Sensors J.*, vol. 14, no. 8, pp. 2792–2800, Aug. 2014, doi: 10.1109/JSEN.2014.2315963.

[14] P. Kassanos, I. F. Triantis, and A. Demosthenous, "A novel front-end for impedance spectroscopy," in *Proc. IEEE Sensors*, Oct. 2011, pp. 327–330, doi: 10.1109/ICSENS.2011.6127367.

[15] S. Hersek *et al.*, "Wearable vector electrical bioimpedance system to assess knee joint health," *IEEE Trans. Biomed. Eng.*, vol. 64, no. 10, pp. 2353–2360, Oct. 2017, doi: 10.1109/TBME.2016.2641958.

[16] R. Pallas-Areny and J. G. Webster, "Bioelectric impedance measurements using synchronous sampling," *IEEE Trans. Biomed. Eng.*, vol. 40, no. 8, pp. 824–829, Aug. 1993, doi: 10.1109/10.238468.

[17] R. Gonzalez-Landaeta, O. Casas, and R. Pallas-Areny, "Heart rate detection from plantar bioimpedance measurements," *IEEE Trans. Biomed. Eng.*, vol. 55, no. 3, pp. 1163–1167, Mar. 2008, doi: 10.1109/TBME.2007.906516.

[18] J. M. Torrents and R. Pallas-Areny, "Compensation of impedance meters, when using an external front-end amplifier," *IEEE Trans. Instrum. Meas.*, vol. 51, no. 2, pp. 310–313, Apr. 2002, doi: 10.1109/19.997829.

[19] *Agilent Impedance Measurement Handbook: A Guide to Measurement Technology and Techniques*, Agilent Technologies, Santa Clara, CA, USA, 2013.

[20] J. M. Torrents and R. Pallas-Areny, "Uncertainty analysis in two-terminal impedance measurements with residual correction," in *Proc. 18th IEEE Instrum. Meas. Technol. Conf.*, 2001, pp. 1450–1453, doi: 10.1109/IMTC.2001.929446.

[21] *Effective impedance Measurement Using OPEN/SHORT/LOAD Correction*. Accessed: Mar. 23, 2017. [Online]. Available: http://web.doe.carleton.ca/~nagui/Appnotes/Agilent/NetworkAnalyzer/5091-6553E.pdf

[22] T. Zagar and D. Krizaj, "An instrumentation amplifier as a front-end for a four-electrode bioimpedance measurement," *Physiol. Meas.*, vol. 28, no. 8, pp. 57–65, Aug. 2007, doi: 10.1088/0967-3334/28/8/N03.

[23] E. Gersing, "Measurement of electrical impedance in organs. Measuring equipment for research and clinical applications," *Biomed. Tech.*, vol. 36, nos. 1–2, pp. 6–11, 1991.

[24] R. Pallas-Areny and J. G. Webster, "AC instrumentation amplifier for bioimpedance measurements," *IEEE Trans. Biomed. Eng.*, vol. 40, no. 8, pp. 830–833, Aug. 1993, doi: 10.1109/10.238470.

[25] P. J. Riu, J. Rosell, A. Lozano, and R. Pallá-Areny, "Multi-frequency static imaging in electrical impedance tomography: Part 1 instrumentation requirements," *Med. Biol. Eng. Comput.*, vol. 33, no. 6, pp. 784–792, Nov. 1995, doi: 10.1007/BF02523010.

[26] A. McEwan, G. Cusick, and D. S. Holder, "A review of errors in multi-frequency EIT instrumentation," *Physiol. Meas.*, vol. 28, no. 7, pp. S197–S215, Jun. 2007, doi: 10.1088/0967-3334/28/7/S15.

[27] K. A. Ng and P. K. Chan, "A CMOS analog front-end IC for portable EEG/ECG monitoring applications," *IEEE Trans. Circuits Syst. I, Reg. Papers*, vol. 52, no. 11, pp. 2335–2347, Nov. 2005, doi: 10.1109/TCSI.2005.854141.

[28] A. Worapishet, A. Demosthenous, and X. Liu, "A CMOS instrumentation amplifier with 90-dB CMRR at 2-MHz using capacitive neutralization: Analysis, design considerations, and implementation," *IEEE Trans. Circuits Syst. I, Reg. Papers*, vol. 58, no. 4, pp. 699–710, Apr. 2011, doi: 10.1109/TCSI.2010.2078850.

[29] J. Rosell and P. Riu, "Common-mode feedback in electrical impedance tomography," *Clin. Phys. Physiol. Meas.*, vol. 13, no. A, pp. 11–14, Dec. 1992, doi: 10.1088/0143-0815/13/A/002.

[30] G. I. Petrova, "Influence of electrode impedance changes on the common-mode rejection ratio in bioimpedance measurements," *Physiol. Meas.*, vol. 20, no. 4, pp. 11–19, Sep. 1999, doi: 10.1088/0967-3334/20/4/401.

[31] S. Grimnes and Ø. G. Martinsen, "Sources of error in tetrapolar impedance measurements on biomaterials and other ionic conductors," *J. Phys. D, Appl. Phys.*, vol. 40, no. 1, pp. 9–14, Jan. 2007, doi: 10.1088/0022-3727/40/1/S02.

[32] G. T. Ong and P. K. Chan, "A power-aware chopper-stabilized instrumentation amplifier for resistive wheatstone bridge sensors," *IEEE Trans. Instrum. Meas.*, vol. 63, no. 9, pp. 2253–2263, Sep. 2014, doi: 10.1109/TIM.2014.2308992.

[33] B. Sanchez, X. Fernandez, S. Reig, and R. Bragos, "An FPGA-based frequency response analyzer for multisine and stepped sine measurements on stationary and time-varying impedance," *Meas. Sci. Technol.*, vol. 25, no. 1, Nov. 2013, Art. no. 015501, doi: 10.1088/0957-0233/25/1/015501.

[34] A. Gabino and J. Spencer. *LTspice: Worst-Case Circuit Analysis with Minimal Simulations Runs|Analog Devices*. Accessed: Apr. 1, 2020. [Online]. Available: https://www.analog.com/en/technical-articles/ltspice-worst-case-circuit-analysis-with-minimal-simulations-runs.html

[35] S. Anastasova, P. Kassanos, and G.-Z. Yang, "Multi-parametric rigid and flexible, low-cost, disposable sensing platforms for biomedical applications," *Biosensors Bioelectron.*, vol. 102, pp. 668–675, Apr. 2018, doi: 10.1016/j.bios.2017.10.038.

[36] D. B. Geselowitz, "An application of electrocardiographic lead theory to impedance plethysmography," *IEEE Trans. Biomed. Eng.*, vols. BME–18, no. 1, pp. 38–41, Jan. 1971, doi: 10.1109/TBME.1971.4502787.

[37] J. C. Williams, J. A. Hippensteel, J. Dilgen, W. Shain, and D. R. Kipke, "Complex impedance spectroscopy for monitoring tissue responses to inserted neural implants," *J. Neural Eng.*, vol. 4, no. 4, p. 410, 2007, doi: 0.1088/1741-2560/4/4/007.

[38] G. C. McConnell, R. J. Butera, and R. V. Bellamkonda, "Bioimpedance modeling to monitor astrocytic response to chronically implanted electrodes," *J. Neural Eng.*, vol. 6, no. 5, Oct. 2009, Art. no. 055005, doi: 10.1088/1741-2560/6/5/055005.

[39] S. F. Lempka, S. Miocinovic, M. D. Johnson, J. L. Vitek, and C. C. McIntyre, "In vivoimpedance spectroscopy of deep brain stimulation electrodes," *J. Neural Eng.*, vol. 6, no. 4, Aug. 2009, Art. no. 046001, doi: 10.1088/1741-2560/6/4/046001.

[40] A. S. Bondarenko and G. A. Ragoisha, *Progress in Chemometrics Research*. New York, NY, USA: Nova Science, 2005, pp. 89–102.

[41] Y.-K. Lo, C.-W. Chang, and W. Liu, "Bio-impedance characterization technique with implantable neural stimulator using biphasic current stimulus," in *Proc. 36th Annu. Int. Conf. Eng. Med. Biol. Soc.*, Aug. 2014, pp. 474–477, doi: 10.1109/EMBC.2014.6943631.

[42] C.-W. Chang, Y.-K. Lo, P. Gad, R. Edgerton, and W. Liu, "Design and fabrication of a multi-electrode array for spinal cord epidural stimulation," in *Proc. 36th Annu. Int. Conf. IEEE Eng. Med. Biol. Soc.*, Aug. 2014, pp. 6834–6837, doi: 10.1109/EMBC.2014.6945198.

[43] P. Kassanos and G. Z. Yang, "A CMOS programmable phase shifter for compensating synchronous detection bioimpedance systems," in *Proc. 24th IEEE Int. Conf. Electron., Circuits Syst. (ICECS)*, Dec. 2017, pp. 218–221, doi: 10.1109/ICECS.2017.8292091.

[44] I. Pachnis, A. Demosthenous, and N. Donaldson, "Towards an adaptive modified quasi-tripole amplifier configuration for EMG neutralization in neural recording tripoles," in *Proc. IEEE Int. Symp. Circuits Syst.*, May 2010, pp. 3144–3147, doi: 10.1109/ISCAS.2010.5537966.

[45] P. Kassanos, A. Demosthenous, and R. H. Bayford, "Optimization of bipolar and tetrapolar impedance biosensors," in *Proc. IEEE Int. Symp. Circuits Syst.*, May 2010, pp. 1512–1515, doi: 10.1109/ISCAS.2010.5537373.

[46] X. Liu, A. Demosthenous, and N. Donaldson, "Platinum electrode noise in the ENG spectrum," *Med. Biol. Eng. Comput.*, vol. 46, no. 10, pp. 997–1003, Oct. 2008, doi: 10.1007/s11517-008-0386-z.

[47] A. Hassibi, R. Navid, R. W. Dutton, and T. H. Lee, "Comprehensive study of noise processes in electrode electrolyte interfaces," *J. Appl. Phys.*, vol. 96, no. 2, pp. 1074–1082, Jul. 2004, doi: 10.1063/1.1755429.

[48] S. F. Lempka *et al.*, "Optimization of microelectrode design for cortical recording based on thermal noise considerations," in *Proc. Int. Conf. IEEE Eng. Med. Biol. Soc.*, Aug. 2006, pp. 3361–3364, doi: 10.1109/IEMBS.2006.259432.

[49] E. T. McAdams, J. Jossinet, R. Subramanian, and R. G. E. McCauley, "Characterization of gold electrodes in phosphate buffered saline solution by impedance and noise measurements for biological applications," in *Proc. Int. Conf. IEEE Eng. Med. Biol. Soc.*, Aug. 2006, pp. 4594–4597, doi: 10.1109/IEMBS.2006.260406.

[50] E. Huigen, A. Peper, and C. A. Grimbergen, "Investigation into the origin of the noise of surface electrodes," *Med. Biol. Eng. Comput.*, vol. 40, no. 3, pp. 332–338, 2002. May 2002, doi: 10.1007/BF02344216.

Panagiotis Kassanos (Member, IEEE) was born in Athens, Greece, in 1983. He received the M.Eng. and Ph.D. degrees in electronic and electrical engineering from the University College London (UCL), London, U.K., in 2006 and 2012, respectively.

From 2010 to 2011, he held a Post-Doctoral EPSRC Ph.D. + Research Fellowship and from 2011 to 2013, he was a Research Associate with the Analog and Biomedical Electronics Group, Department of Electronic and Electrical Engineering, UCL. From 2013 to 2014, he was an Honorary Research Associate with the Biomedical Engineering Research Group, Department of Electrical and Electronic Engineering, City University of London, London. He is currently a Research Associate with The Hamlyn Centre for Robotic Surgery, Imperial College London, London. His current research interests include analog and mixed-signal integrated circuits for biomedical, sensor and signal processing applications, electrochemical sensors, embedded systems and instrumentation, microfluidics, sensor design and fabrication, flexible/stretchable electronics, and low-cost fabrication techniques.

Florent Seichepine was born in Belfort, France, in 1985. He received the engineering degree in material science and the M.Sc. degree in nanomaterials from the University of Toulouse, Toulouse, France, in 2008, and the Ph.D. degree in nanophysics from the University of Toulouse, Toulouse, France, in 2011.

During Ph.D. research, he focused on carbon nanotube interconnection, while working for the CNRS, Toulouse, and INTEL Ireland, Leixlip, Ireland. From 2012 to 2016, he was a Research Assistant with the Frey Initiative Research Unit, RIKEN, Kobe, Japan. He joined The Hamlyn Centre for Medical Robotic, Imperial College London, London, U.K., as a Research Associate, in 2016, where he is also the Head of the Centre's research facilities. His research is mainly focused on microfabrication, packaging, and the use of nanomaterials for electronics and sensing in biological environments. He currently pursues research on implantable and wearable sensors for medical applications and fabrication of microrobots.

Guang-Zhong Yang (Fellow, IEEE) received the Ph.D. degree in computer science from Imperial College London, London, U.K., in 1991.

He was the Director of The Hamlyn Centre for Robotic Surgery, Imperial College London, London, U.K., from 1999 to 2019. He is currently the Dean of the Institute of Medical Robotics, Shanghai Jiao Tong University, Shanghai, China.

Dr. Yang is a fellow of the Royal Academy of Engineering, IET, AIMBE, IAMBE, MICCAI, BSN, and City of Guilds. He was a recipient of the Royal Society Research Merit Award and The Times Eureka "Top 100" in British Science. He was the Editor-in-Chief of the IEEE JOURNAL OF BIOMEDICAL AND HEALTH INFORMATICS. He is currently the Editor of the *Science Robotics*. He is a Distinguished Lecturer of the IEEE Engineering in Medicine and Biology Society.